Shaped Antenna Designs and Performance for 64-m Class DSN Antennas

P. D. Potter
Communications Elements Research Section

Significant DSN antenna performance enhancement is possible through the use of shaped dual reflector antenna techniques. A detailed study has been performed to optimize configurations for maximum performance. Four designs in the antenna diameter size range of 64 to 72 m were carried out and are reported here. Complete performance predictions and mechanical configurations are given.

I. Introduction

Several possibilities exist for enhancement of the gain and noise temperature performance of the Deep Space Network (DSN) 64-m class antennas. The DSS 14 antenna noise temperature degradation due to quadripod scatter has been recently calibrated (Ref. 1), a possible technique for performance improvement has been proposed (Ref. 2) and related field tests are presently being performed at DSS 13. This article deals with possible improvement of antenna aperture efficiency (and hence gain) and reduction of spillover noise contribution by use of reflector surface shaping.

For two-reflector quasi-Cassegrain antennas, a technique was developed by Galindo (Refs. 3, 4) for achievement of almost 100% aperture efficiency by use of specially-shaped reflector surfaces to transform the (arbitrary) feed radiation pattern into a uniformly (in amplitude and phase) illuminated antenna aperture. The Galindo technique uses geometric optics to solve the reflector surface simultaneous differential equations such that the feed radiation pattern is transformed into uniform aperture illumination. Being optical, the resulting solution is essentially frequency independent. The Galindo method was reduced to practice some time ago by Williams (Ref. 5) and its possible application to the DSS 14 64-m antenna was studied by Ludwig (Ref. 6). The Galindo technique has also been successfully used by numerous other organizations to realize ultrahigh aperture efficiency in ground antennas.

All of the above shaped antenna designs involve antenna surfaces that are figures of revolution. With the DSN 64-m antenna asymmetric tricone feed system, such

designs are not applicable. The general case of arbitrary shaped dual reflector systems has been studied by Yeh (Ref. 7) and results in a set of extremely complex nonlinear partial differential equations to be solved. A further difficulty is that the DSN antenna tricone concept is such that the main reflector must be a figure of revolution.

An approximate asymmetric shaping technique that circumvents the above difficulties has been recently developed by Potter (Ref. 2). This method is optical and involves a perturbation of the symmetric surfaces generated by the standard Galindo method. The main reflector is left unperturbed and a minimum perturbation of the subreflector is made to maintain constant path length for all system rays. The result of this process is uniform, frequency-independent aperture phase and an aperture amplitude that is slightly asymmetric. The resulting asymmetry gain loss is, however, small (about 0.1 dB for the DSN antenna geometry).

In this article, the results of a detailed shaping design study are presented. Shaped designs were synthesized for DSN antenna diameters of 64 m, 68 m, 70 m, and 72, and are presented here. Performance level was analyzed in detail and is also presented. The following section discusses the design method.

II. Design Method

Figure 1 shows the shaped antenna geometry. Because of the finite wavelength of operation and the requirement for ultralow noise performance (low rear spillover) the outer part of the main reflector is in reality a "noise shield." The optical edge of the symmetrically shaped main reflector thus exists at a radius *XMAX*, where $XMAX < DMAIN/2$. Visualizing the antenna as receiving an axial signal, an incoming ray that strikes the main reflector at a radius of *XMAX* is reflected at an angle β_E and is directed towards the point 0. All such rays lie in a right circular cone of semiangle β_E, as shown in Fig. 1. These cone rays are intercepted by the asymmetric subreflector, whose edge also lies in this conical surface, and are directed to the feed at the point *P*. The subreflector surface is mathematically constructed such that all other axial rays that strike the main reflector within a radius of *XMAX* also focus to the point *P*.

The noise shield angle $(\Psi_2 - \Psi_1)$ is determined by the diffraction characteristic of the subreflector at the design frequency. Visualizing the antenna as being in the transmitting mode, the phase characteristic of the scattered field changes rapidly near the cutoff at XMAX. To constructively use the energy between *XMAX* and $DMAIN/2$, the surface is shaped to fit the scattered field phase characteristic at the design frequency. It actually turns out to be necessary to do nonoptical surface modification somewhat inside the radius *XMAX*.

Figures 2(a) and (b) show, respectively, the design procedure that was used and the associated JPL computer software for performing the calculations. Considering Fig. 2(a) first, step 1 consists of making certain fundamental decisions; in this case antenna diameters of 64, 68, 70 and 72 m, a subreflector size of 6.096 m (20 ft.), the existing feedhorn phase center location, and a forward spillover of 1%.

The JPL hybrid horn computer program (Ref. 8) has demonstrated the ability to exactly predict antenna feedhorn radiation patterns as a function of physical geometry and was used in step 2 of Fig. 2(a). The required feedhorn is approximately twice as large as the presently-used DSN hybrid-mode feedhorn. This size would not pose a serious problem at X-band, but would probably require some other approach (such as reflex optics) at S-band. Attempts to reduce horn length by flare-angle increase were unsuccessful, resulting in an unacceptable horn sidelobe level and phase distortion of the pattern. The Cramer efficiency program was used to integrate the horn radiation pattern and determine forward spillover level. Figure 3 shows the final horn design dimensions and radiation pattern at 8.450 GHz.

The symmetrical ($R_D = 0$ in Fig. 1), shaped subreflector was designed with the Galindo-method Ludwig shaping program, and the feedhorn-subreflector scattered fields were evaluated with the Rusch physical-optics scattering program. Figures 4, 5, and 6 show, respectively, the existing DSS 14 X-band scattered pattern, a quasi-uniformly-illuminated subreflector test case, and the final symmetrical shaped subreflector scattered pattern at X-band. In deriving the system whose pattern is shown in Fig. 6, the Cramer efficiency program was utilized to evaluate antenna efficiency and rear spillover vs the cutoff angle β_E (see Fig. 1), and the design was iterated (two tries, actually) until satisfactory performance was achieved. A tricky parallax problem arises here, however. The subreflector is so large that the main reflector is in its near field. The actual fields in the vicinity of the main reflector edge may be calculated, in principle, using spherical wave techniques (Ref. 9). The associated parallax problem can be seen with reference to Fig. 1. The fields at the main reflector edge are absolute, independent

of radiation pattern origin. On the other hand, the radiation pattern cutoff angle clearly depends on the origin choice.

To calculate the true near-field spillover level, the X-band scattered pattern was expanded in modal waves with the Cramer expansion program. It was discovered that a maximum order of 170 waves could be used before serious numerical difficulties developed. This restriction resulted in a poor fit to the input pattern with only 99.2% of the input pattern power being accounted for. Figure 7 shows the total mode energy vs maximum order for this and also an S-band scattered pattern (Fig. 8). For the latter, an excellent fit was obtained. Figure 8 shows clearly the parallax effect at S-band. In the vicinity of the edge cutoff, the near-field pattern is shifted by approximately 1.3 deg. A spillover analysis of the near- and far-field S-band pattern shows the same spillover results for an angular displacement (relative to a focal point, F, origin) of 2.9 deg. This is in fair agreement with the value of 2.794 deg for $(\Psi_1 - \beta_E)$. An anticipated future effort is to upgrade the spherical wave software so that X-band near-field effects can be accurately analyzed.

The Potter asymmetric shaping/scattering program generates the required asymmetric subreflector surface and then calculates the scattered pattern using two-dimensional numerical integration. By using a symmetric configuration (a special case for the program) and comparing results against the Rusch symmetric scattering program, the required number of integration points was determined. It was determined that the program, which uses the Ludwig integration algorithm (Ref. 10) required 40 polar and 80 azimuthal integration points to reduce errors to a -40-dB level. This integration grid corresponds to a polar point spacing of 0.6 wavelength and checks with previous studies of the Ludwig algorithm (Ref. 11). The resulting S-band asymmetric scattering run machine time for the Univac 1108 was 27 min (31 polar $\times$ 7 azimuthal observation points). This time amounts to approximately 2 ms per point, which is typical for this type of program on the Univac 1108. The overall result of these tests is that X-band asymmetric scattering runs are not economically feasible.

Figure 9 shows the S-band asymmetric scattered patterns; as expected a certain amount of amplitude asymmetry is present. The degree of the asymmetric effect is determined with the azimuthal Fourier program (see Ref. 12 for a discussion of the theory and application of this method). As with the reflex feed (Ref. 12) the primary contributors to the asymmetry are the $m = 0$ and $m = 2$ components (both approximately -20 dB relative to the desired $m = 1$ component). Figure 10 shows the $m = 1$ component (this component alone contributes to the axial antenna gain) radiation pattern. This pattern turns out to be virtually identical to the pattern of a symmetric shaped system (Fig. 8).

The asymmetric effects introduced by the subreflector (0.1-dB gain/loss) are expected to be essentially frequency independent, since the design is optical. Thus asymmetric X-band performance may be established from a combination of symmetric X-band and asymmetric S-band computations, thereby avoiding the necessity for expensive asymmetric X-band scattering calculations.

Having designed and optimized the system optics for X-band, it remained to optimize the S-band illumination. Figures 11 and 12 show the symmetric S-band far-field scattered patterns for feed apertures scaled up by ratios of 1.25 and 1.50, respectively, from the X-band design. From a rear spillover standpoint, it appears that the 1.25 case is desirable (see Table 2 below).

In the following section the computed performance data are presented.

III. Computed Performance

Table 1 shows the computed performance for the X-band shaped system and for the existing DSS 14 X-band system. In the case of the shaped system amplitude illumination factor, a rather large tolerance is assigned because of the near-field parallax problem discussed above. It is expected that future JPL spherical wave software improvement will enable a more exact calculation of this parameter. The overall result is an X-band gain improvement from shaping of approximately 0.7 dB.

Table 2 shows the computed shaped system performance at S-band for three feed sizes and for the existing DSS 14 standard feed. A shaping improvement of approximately 0.5 dB (aperture ratio 1.25) is predicted.

All of the design optimization and performance evaluation was done for a main reflector diameter of 68 m, which is centered in the study range of 64- to 72-m diameter. Aperture efficiency and spillover performance is expected to be completely insensitive to the diameter. Actual mechanical configurations for each antenna diameter are given in the following section.

IV. Mechanical Configuration

The geometrical configuration parameters are defined in Figs. 1 and 13. Table 3 gives the values for the parameters for the selected four antenna diameters.

V. Conclusions

Using a set of very sophisticated JPL software, detailed shaped antenna designs have been performed for diameters of 64 m, 68 m, 70 m, and 72 m; the associated performance has been computed. Relative to the existing DSS 14 64-m antenna system, X-band forward spillover has been reduced from 5.5% to 1%, rear spillover has been reduced from 0.2% to 0.04%, and aperture efficiency has been increased by 0.7 dB.

At S-band, forward spillover has been reduced from 5.5% to 0.4%, rear spillover has been reduced from 0.3% to 0.04%, and aperture efficiency has been increased by 0.5 dB.

Complete main reflector/subreflector/feed configuration geometry is presented. The configurations are compatible with the existing tricone system but would require quadripod modification to fit the shaped subreflector.

The performance enhancement data presented here do not include possible reduction of aperture blockage that might be achieved with the required new quadripod design. It is to be noted (Tables 1 and 2) that the existing quadripod aperture efficiency degradation (0.6 dB) is approximately the same as the possible enhancement due to shaping. The quadripod degradation of system noise temperature, expressed in decibels, is several times this large. Thus it appears that an implementation of shaping would logically be combined with a new low-blockage quadripod design.

References

1. Potter, P. D., "Efficient Antenna Systems: Calibration of the Mars Deep Space Station 64-m Antenna System Noise Temperature Degradation Due to Quadripod Scatter", in *The Deep Space Network Progress Report*, Technical Report 32-1526, Vol. XVI, pp. 22–29. Jet Propulsion Laboratory, Pasadena, Calif., Aug. 15, 1973.

2. Potter, P. D., "Antenna Study: Performance Enhancement", in *The Deep Space Network Progress Report*, Technical Report 32-1526, Vol. X, pp. 129–134. Jet Propulsion Laboratory, Pasadena, Calif , Aug. 15, 1972.

3. Galindo, V., *Synthesis of Dual Reflector Antennas*, Report No. 64-22. Electronics Research Laboratory, University of California, Berkeley, Calif., July 1964.

4. Galindo, V., "Design of Dual-Reflector Antennas With Arbitrary Phase and Amplitude Distributions", *IEEE Trans. on Ant. and Prop.*, Vol. AP-12, pp. 403–408, 1964.

5. Williams, W. F., "High Efficiency Antenna Reflector", *Microwave Journal*, pp. 79–82, July 1965.

6. Ludwig, A. C., "Antennas for Space Communication: Shaped Reflector Cassegrainian Antennas", in *Supporting Research and Advanced Development*, Space Programs Summary 37-35, Vol. IV, pp. 266–268. Jet Propulsion Laboratory, Pasadena, Calif., October 31, 1965.

7. Yeh, C., *Arbitrarily Shaped Dual-Reflector Antennas*, Technical Report 32-1503. Jet Propulsion Laboratory, Pasadena, Calif., May 1, 1971.

8. Potter, P. D., "Efficient Antenna Systems: A New Computer Program for the Design and Analysis of High-Performance Conical Feedhorns", in *The Deep Space Network Progress Report*, Technical Report 32-1526, Vol. XIII, pp. 92–107. Jet Propulsion Laboratory, Pasadena, Calif., Feb. 15, 1973.

9. Ludwig, A. C., "Near-Field Far-Field Transformations Using Spherical-Wave Expansions", *IEEE Trans. on Ant. and Prop.*, Vol. AP-19, No. 2, pp. 214–220, Mar. 1971.

10. Ludwig, A. C., "Computation of Radiation Patterns Involving Numerical Double Integration", *IEEE Trans. on Ant. and Prop.*, Vol. AP-16, No. 6, pp. 767–769, Nov. 1968.

11. Brunstein, S. A., Cormack, R. E., and Ludwig, A. C., "Accuracy of Numerically Computed Electromagnetic Scattered Patterns", in *Supporting Research and Advanced Development*, Space Programs Summary 37-52, Vol. III, pp. 233–238. Jet Propulsion Laboratory, Pasadena, Calif., August 1968.

12. Potter, P. D., "S- and X-Band RF Feed System", in *The Deep Space Network Progress Report*, Technical Report 32-1526, Vol. VIII, pp. 53–60. Jet Propulsion Laboratory, Pasadena, Calif., April 15, 1972.

13. Potter, P. D., "S- and X-Band RF Feed System", in *The Deep Space Network Progress Report*, Technical Report 32-1526, Vol. IX, pp. 141–146. Jet Propulsion Laboratory, Pasadena, Calif., June 15, 1972.

Table 1. Computed performance, 8.450 GHz

Factor	Standard feed, 64 m		Shaped system, 68 m	
	Ratio	dB	Ratio	dB
Forward spillover	0.94470	−0.2471	0.98980	−0.0445
Rear spillover	0.99826	−0.0076	0.99965	−0.0015
Nonuniform amplitude illumination	0.84737	−0.7193	0.92965	−0.3168 (±0.2 dB)
Nonuniform phase illumination	0.97175	−0.1244	0.99337	−0.0289
Cross-polarization	0.99994	−0.0003	1.00000	−0.0000
Energy ($m \neq 1$)	0.99805	−0.0085	0.97808	−0.0963
Central blockage	0.94407	−0.2500	0.96866	−0.1383
Quadripod blockage[a]	0.87498	−0.5800	0.87498	−0.5800
Main reflector/subreflector surface tolerance loss (0.1524 cm rms)[b]	0.74748	−1.2640	0.74748	−1.2640
Total	0.47851	−3.2012	0.56620 ±.025	−2.4703 ±0.2
Gain for 100% efficiency	3.211676×10^7	+75.0673	3.625681×10^7	+75.5939
Gain	1.536819×10^7	+71.8661	2.052860×10^7 $\pm .097 \times 10^7$	+73.1236 ±0.2

[a]Possible small change with illumination and quadripod modification unknown.
[b]Possible small change with illumination, and subreflector change and diameter increase unknown.

Table 2. Computed performance, 2.295 GHz

Factor	Standard feed, 64 m[a]		Shaped feed, 68 m					
			Relative aperture size, 1.00[b]		Relative aperture size, 1.25[b]		Relative aperture size, 1.50[b]	
	Ratio	dB	Ratio	dB	Ratio	dB	Ratio	dB
Forward spillover	0.94470	−0.2471	0.98980	−0.0445	0.99602	−0.0173	0.99846	−0.0067
Rear spillover	0.99738	−0.0114	0.99718	−0.0123	0.99957	−0.0019	0.99929	−0.0031
Nonuniform amplitude illumination	0.84207	−0.7465	0.96157	−0.1702	0.89165	−0.4980	0.83234	−0.7970
Nonuniform phase illumination	0.97999	−0.0878	0.98305	−0.0742	0.96358	−0.1611	0.97154	−0.1254
Cross-polarization	0.99982	−0.0008	1.00000	−0.0000	1.00000	−0.0000	1.00000	−0.0000
Energy ($m \neq 1$)	0.99805[c]	−0.0085[c]	0.97808[c]	−0.0963[c]	0.98741[d]	−0.0550[d]	0.99369[d]	−0.0275[d]
Central blockage	0.94148	−0.2619	0.97009	−0.1319	0.96140	−0.1710	0.95271	−0.2104
Quadripod blockage[e]	0.87498	−0.5800	0.87498	−0.5800	0.87498	−0.5800	0.87498	−0.5800
Main reflector/subreflector surface tolerance loss (0.1524 cm rms)[f]	0.97876	−0.0932	0.97876	−0.0932	0.97876	−0.0932	0.97876	−0.0932
Total	0.62557	−2.0372	0.75812	−1.2026	0.69541	−1.5775	0.65414	−1.8433
Gain for 100% efficiency	2.366795×10^6	+63.7416	2.671890×10^6	+64.2682	2.671890×10^6	+64.2682	2.671890×10^6	+64.2682
Gain	1.480608×10^6	+61.7044	2.025613×10^6	+63.0656	1.858059×10^6	+62.6907	1.747790×10^6	+62.4249

[a]From Ref. 13.
[b]Feed wavelength aperture size relative to 8.450 GHz shaped system.
[c]Computed.
[d]Estimated.
[e]Possible small change with illumination and quadripod illumination unknown.
[f]Possible small change with illumination, subreflector change and diameter increase unknown.

Table 3. Geometrical parameters

Parameter value	$DMAIN = 64$ m	$DMAIN = 68$ m	$DMAIN = 70$ m	$DMAIN = 72$ m
XMAX, cm	3029.003 (1192.521 in.)	3283.151 (1292.579 in.)	3320.186 (1307.160 in.)	3417.245 (1345.372 in.)
YMAX, cm	846.099 (333.110 in.)	994.039 (391.354 in.)	1016.591 (400.233 in.)	1076.896 (423.975 in.)
A, cm	−497.383 (−195.820 in.)	−349.674 (−137.667 in.)	−327.119 (−128.787 in.)	−266.611 (−104.965 in.)
β_E, deg	55.4327	59.5972	60.1938	61.7299
Z_{02}, cm	1265.959 (498.409 in.)	1273.589 (501.413 in.)	1274.361 (501.717 in.)	1277.252 (502.855 in.)
RADIUS 1, cm	293.779 (115.661 in.)	292.930 (115.327 in.)	292.875 (115.305 in.)	292.410 (115.122 in.)
RADIUS 2, cm	321.940 (126.748 in.)	323.553 (127.383 in.)	323.875 (127.510 in.)	324.330 (127.689 in.)
ΔZ1, cm	121.158 (47.700 in.)	131.282 (51.686 in.)	132.837 (52.298 in.)	136.512 (53.745 in.)
ΔZ2, cm	101.755 (40.061 in.)	113.314 (44.612 in.)	115.080 (45.307 in.)	119.344 (46.986 in.)

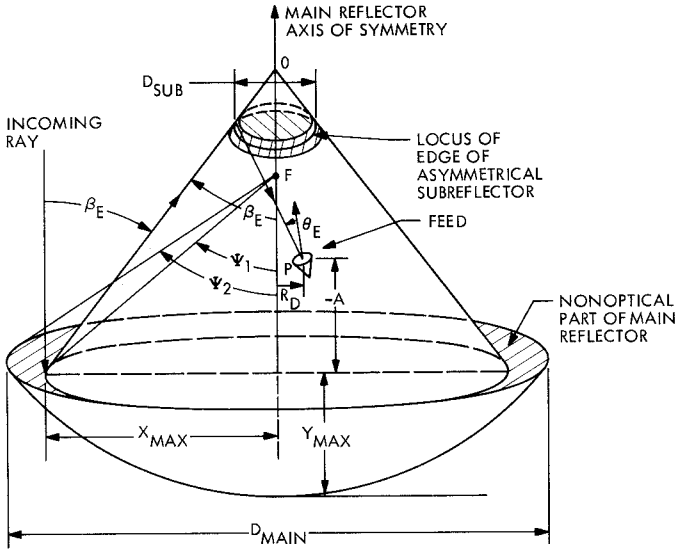

Fig. 1. Asymmetric, shaped antenna system geometry

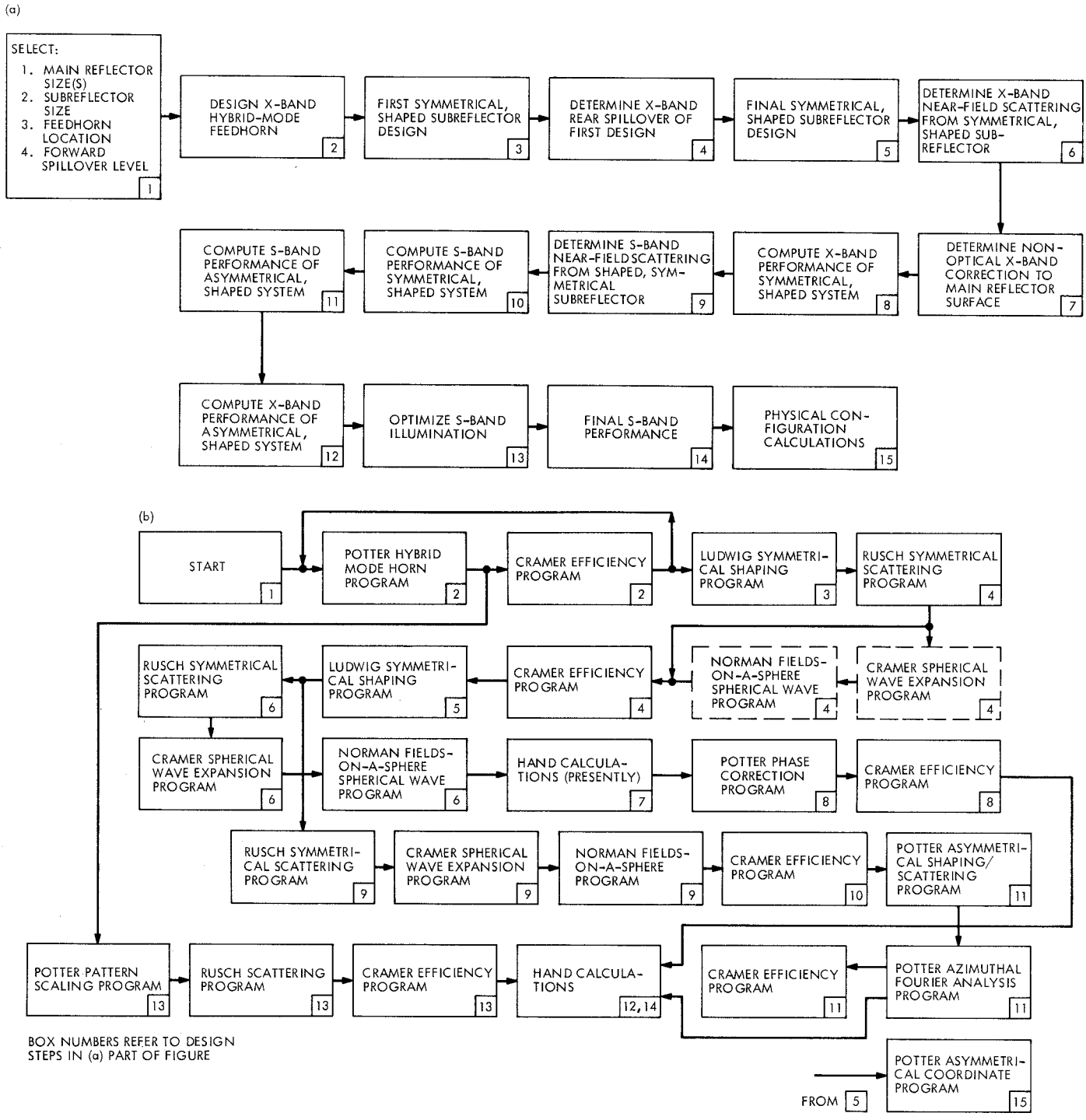

Fig. 2. Multifrequency asymmetrical antenna system design; (a) procedure, (b) computational method

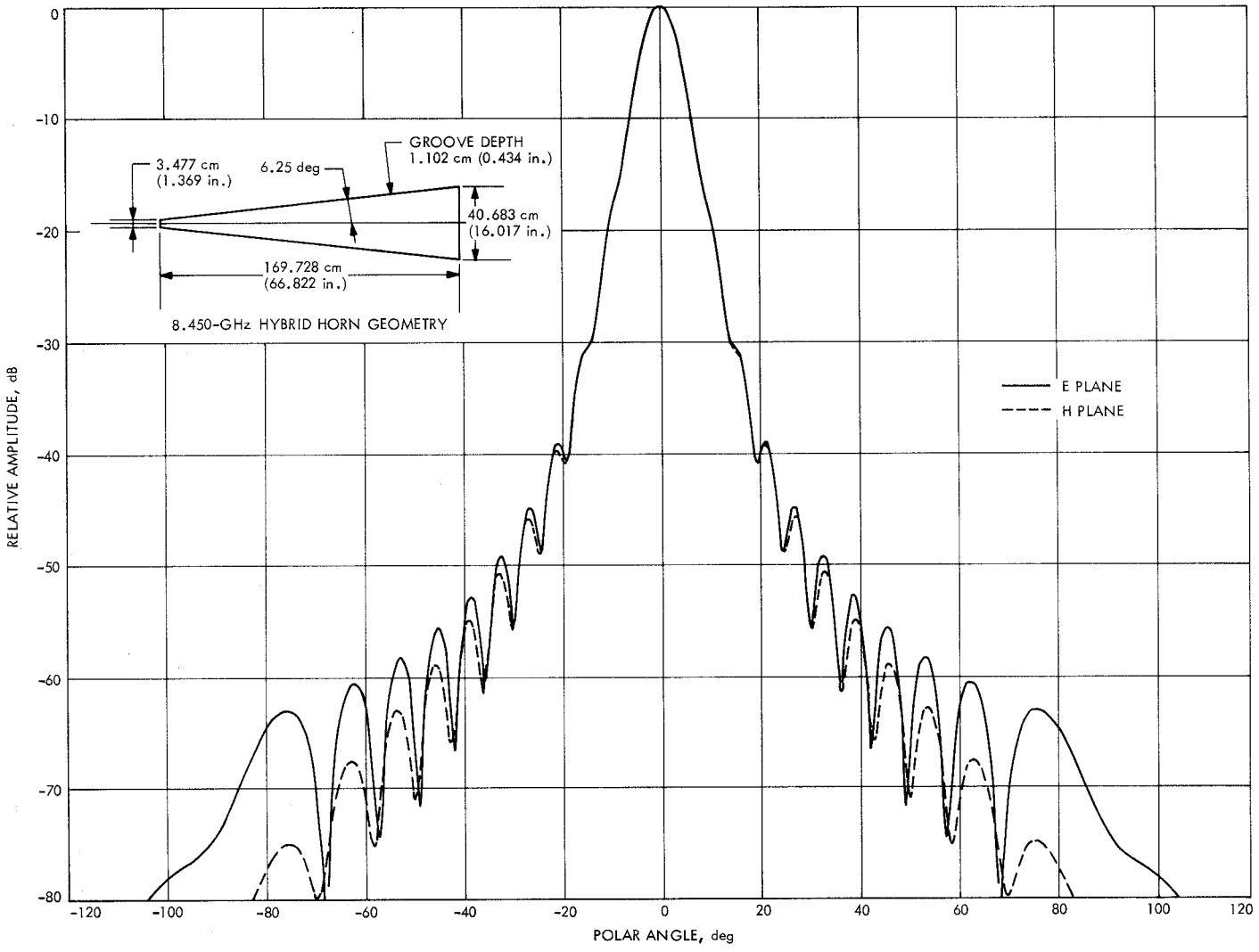

Fig. 3. Hybrid mode feedhorn radiation pattern

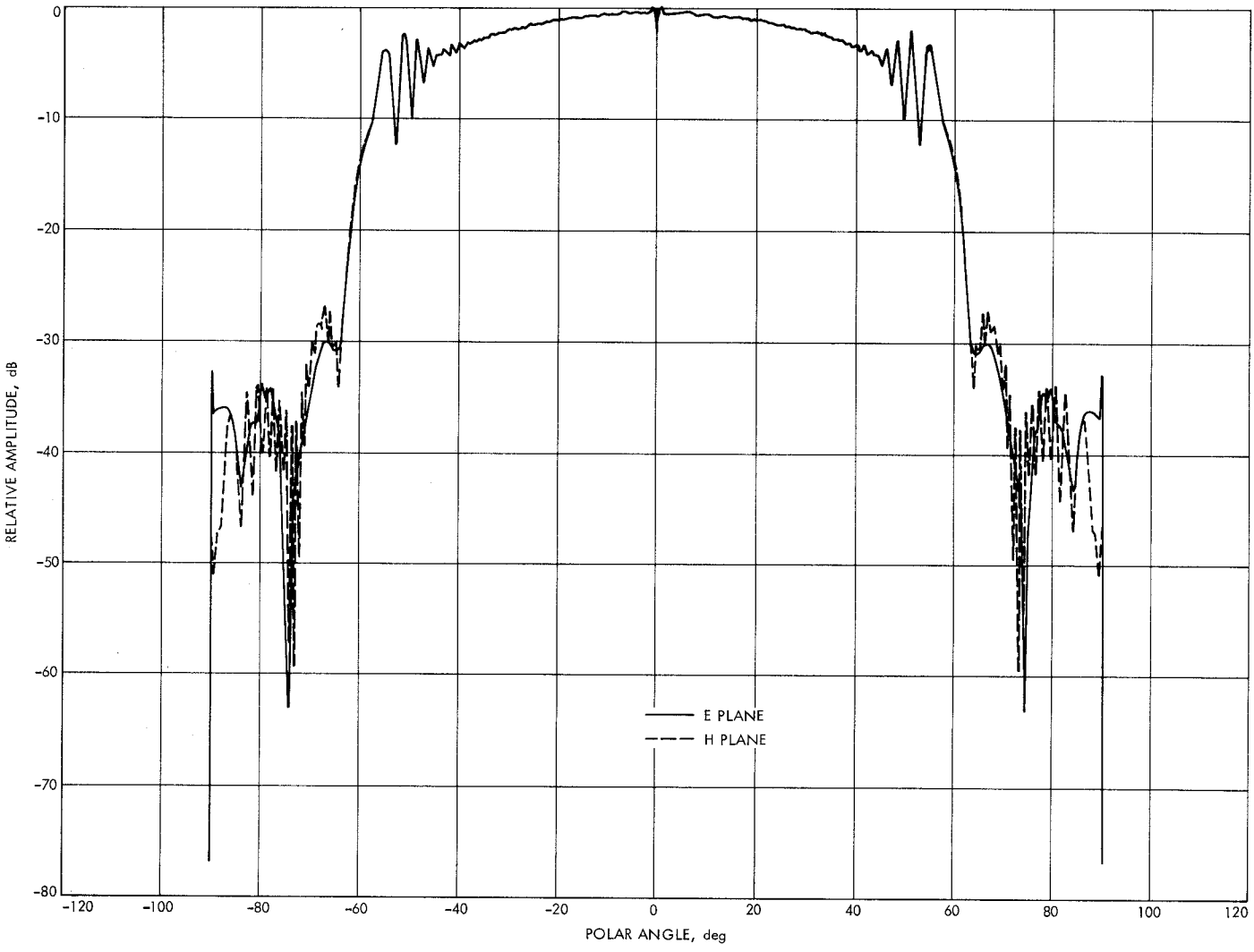

Fig. 4. 8.450-GHz scattered pattern for symmetrical equivalent to existing 64-m antenna feed

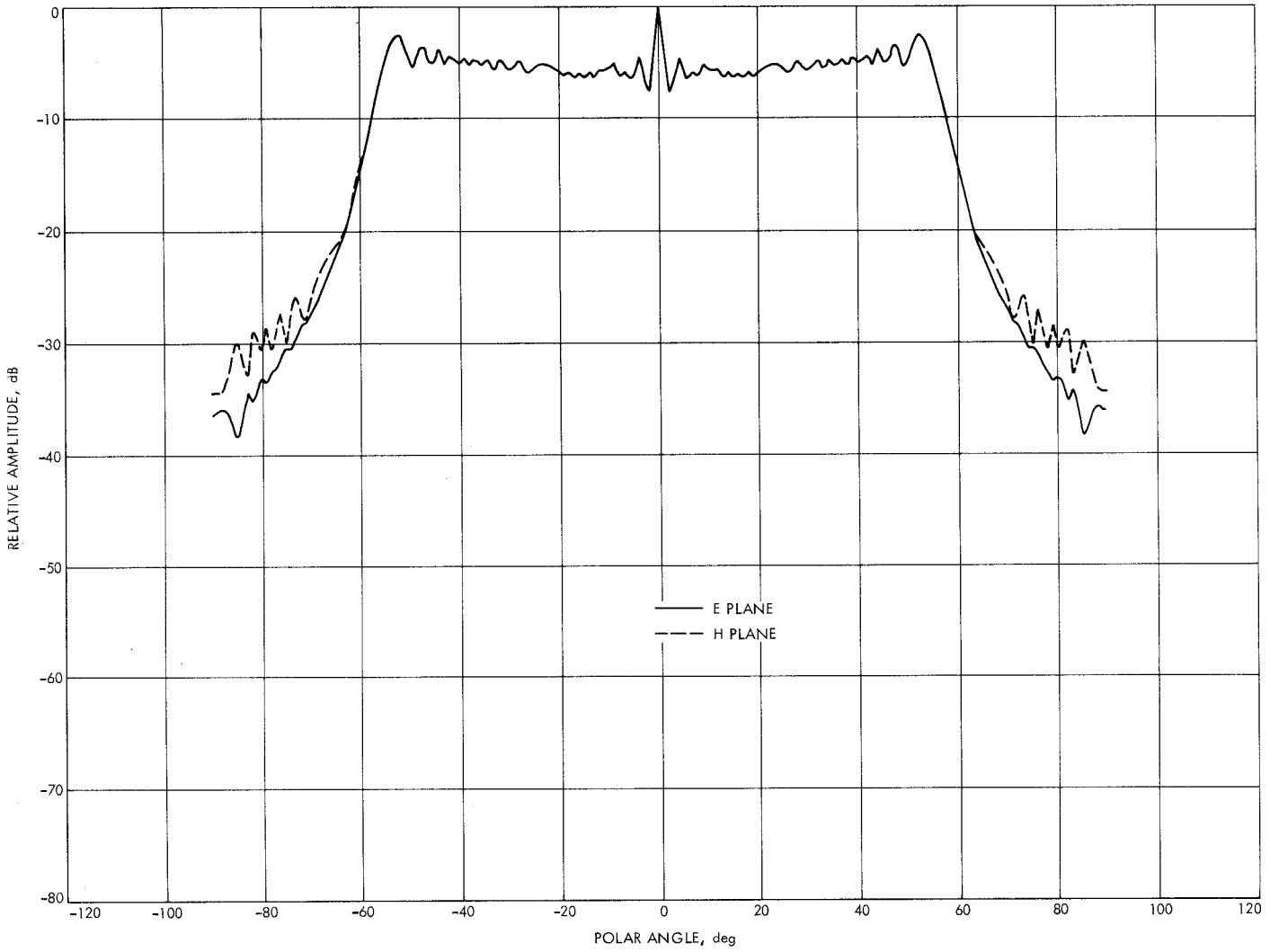

Fig. 5. 8.450-GHz uniform illumination test case

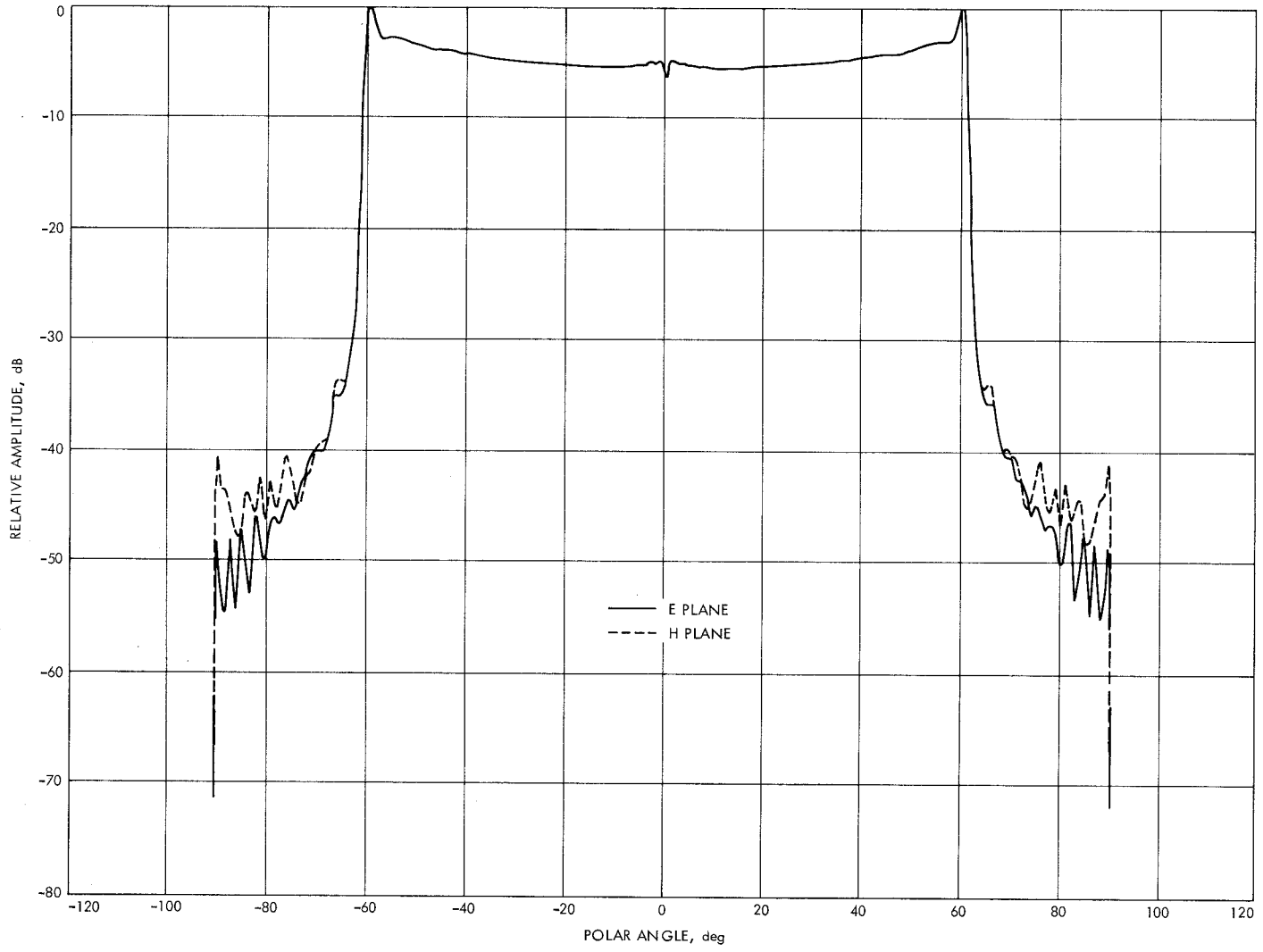

Fig. 6. Shaped system 8.450-GHz far-field radiation pattern

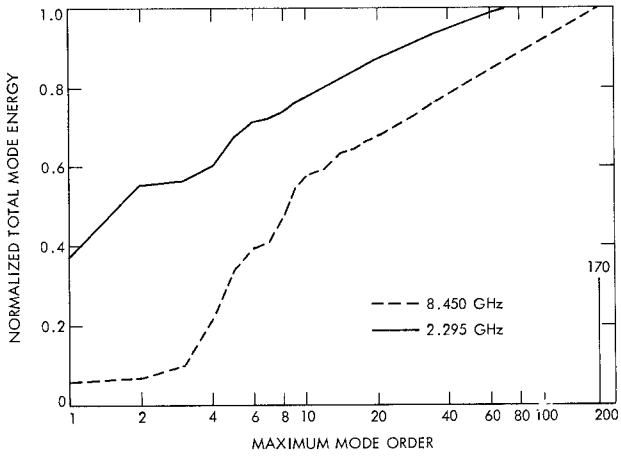

Fig. 7. Spherical wave expansion total mode energy vs maximum mode order

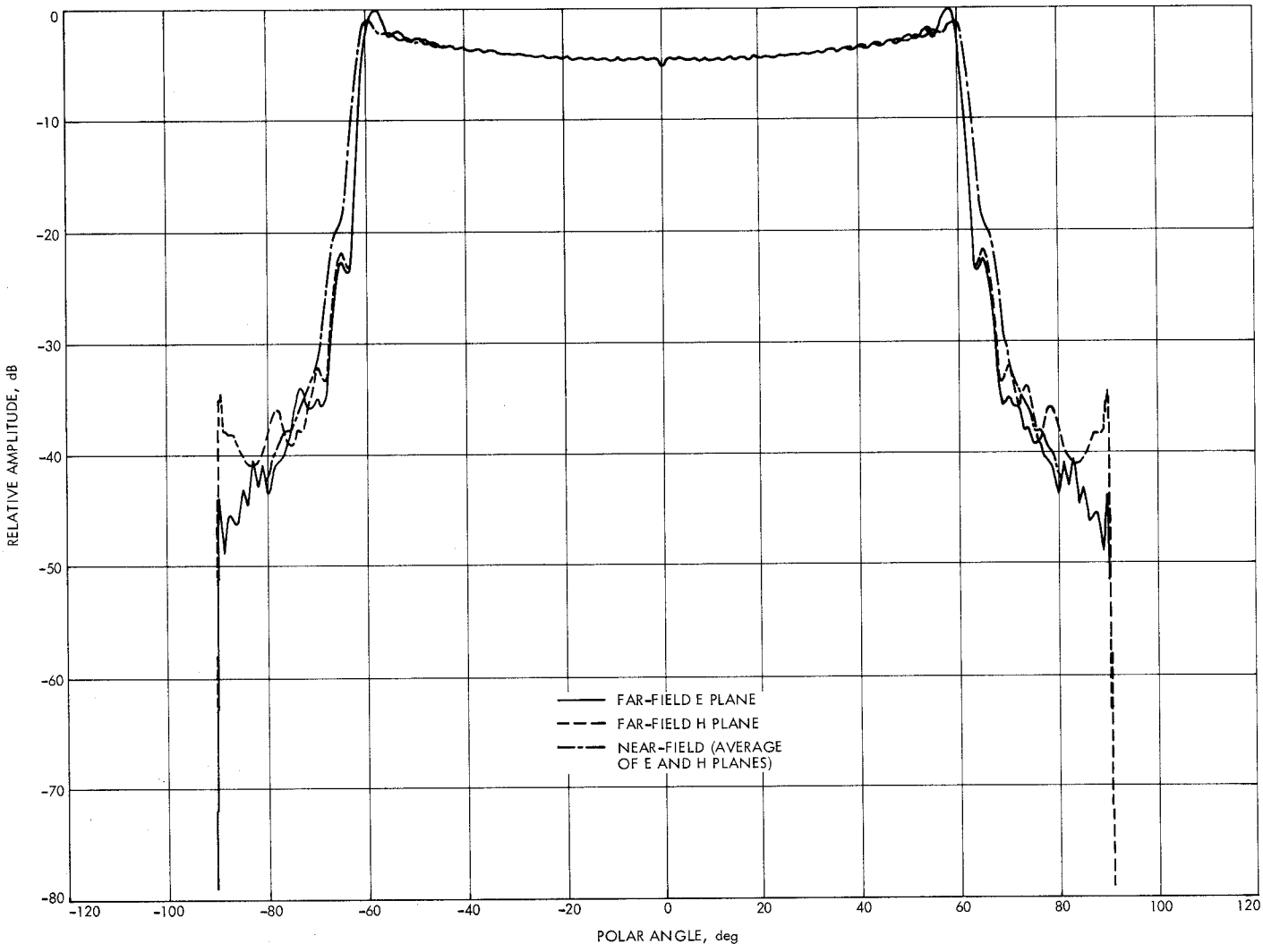

Fig. 8. Near and far-field 2.295-GHz shaped system radiation patterns

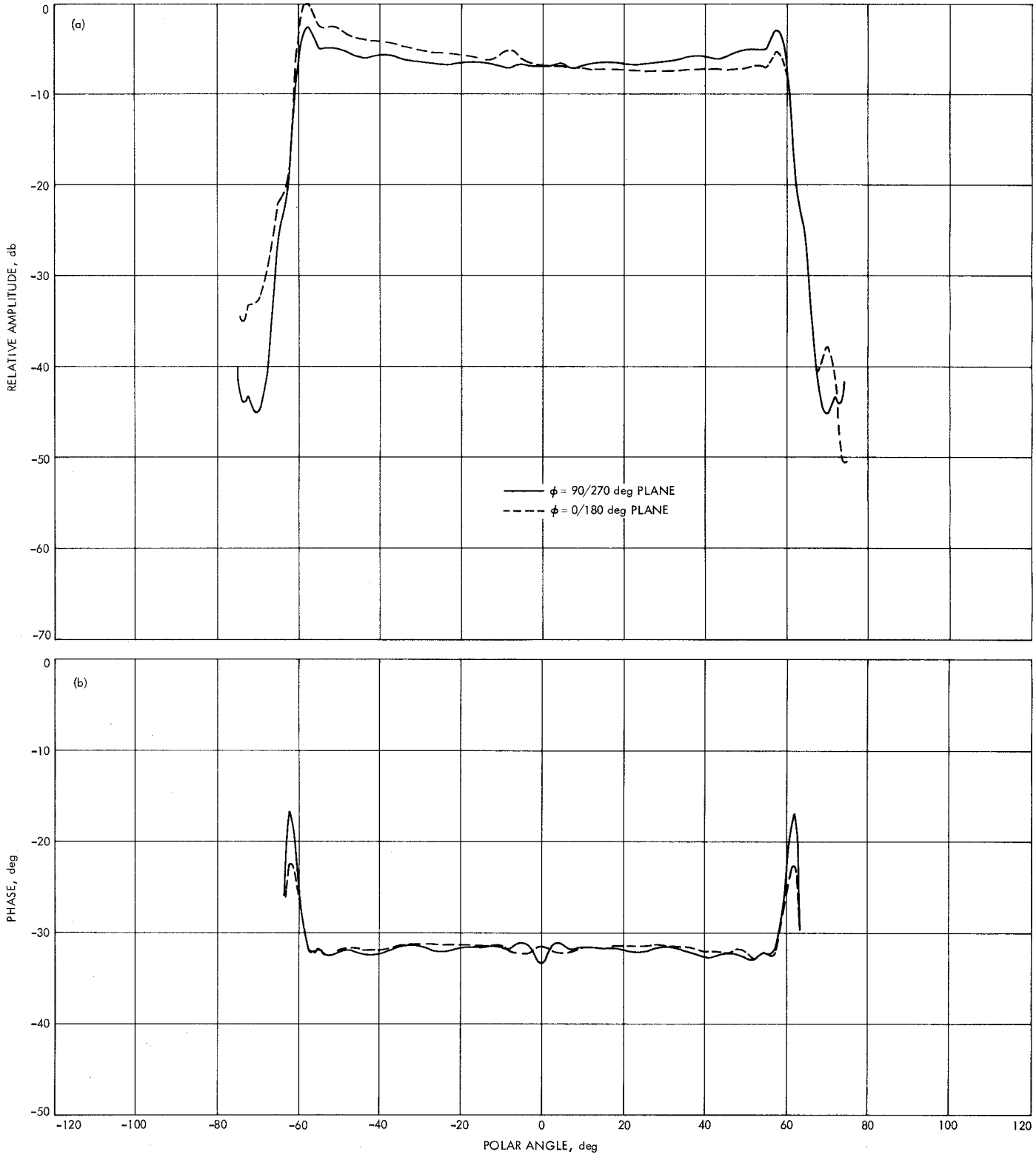

Fig. 9. 2.295-GHz asymmetric, shaped system radiation patterns; (a) amplitude, (b) phase

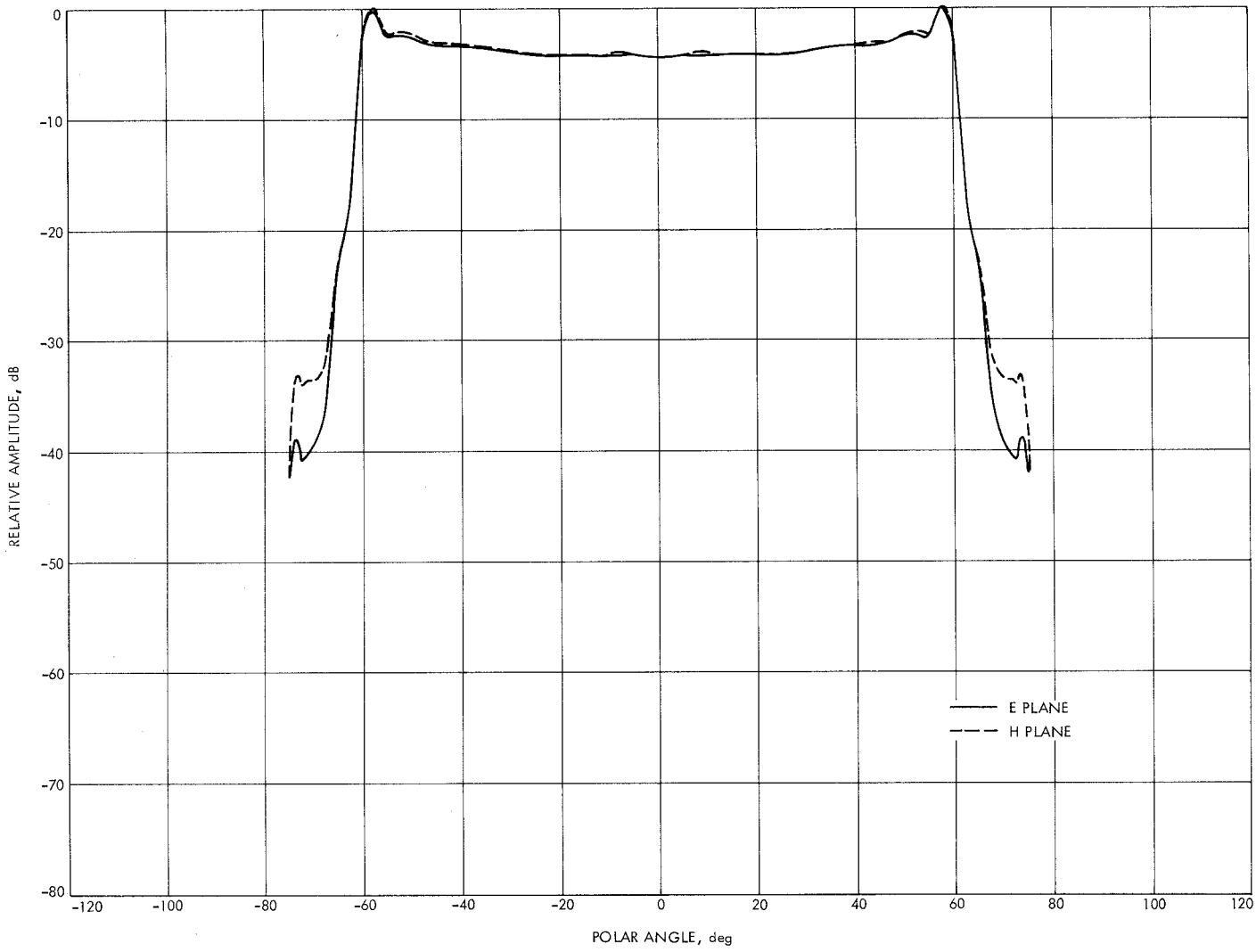

Fig. 10. 2.295-GHz ($m = 1$) component of asymmetric, shaped system radiation patterns

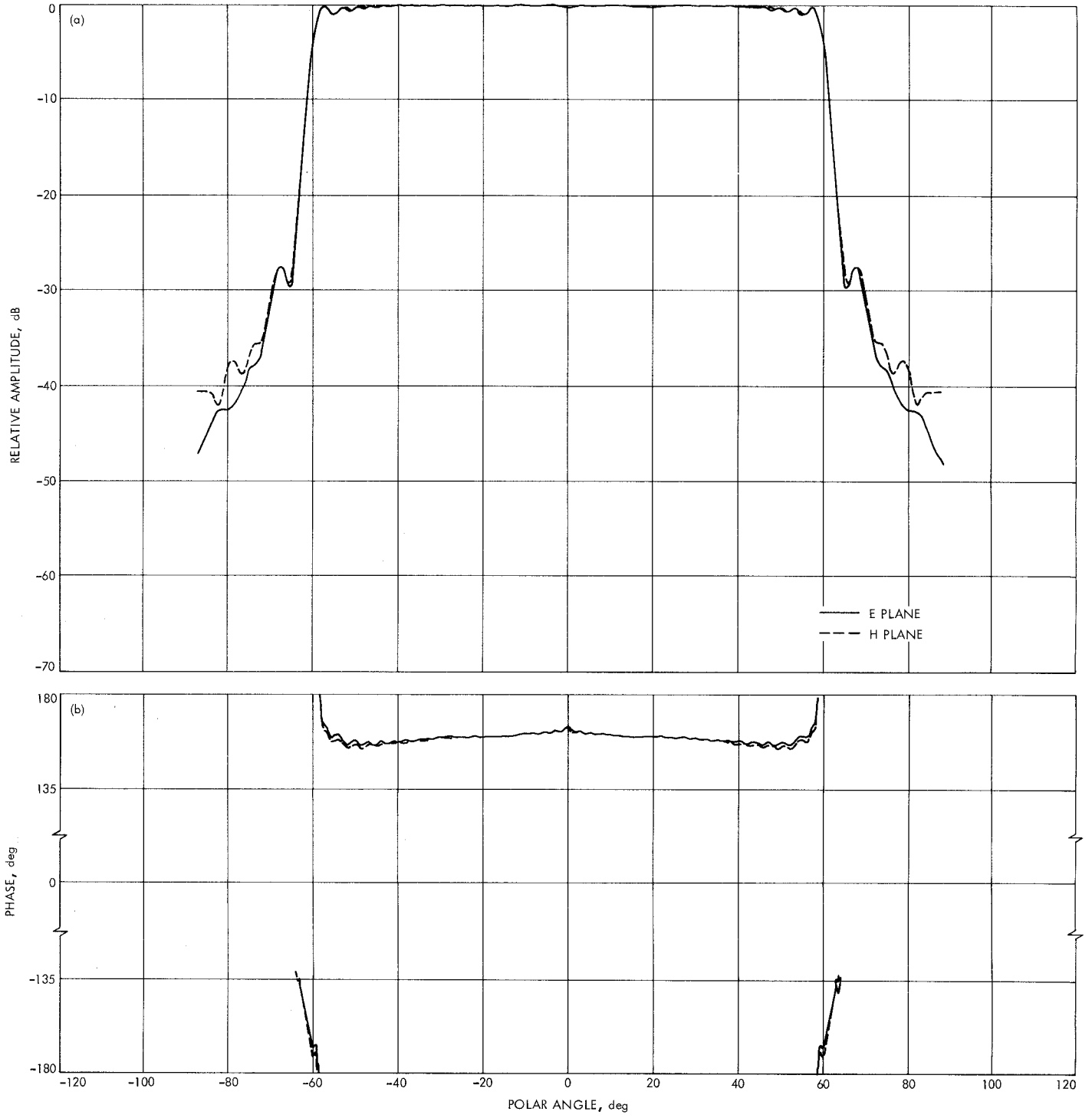

Fig. 11. 2.295-GHz symmetric, shaped system with illuminating aperture scaled by 1.25; (a) amplitude, (b) phase

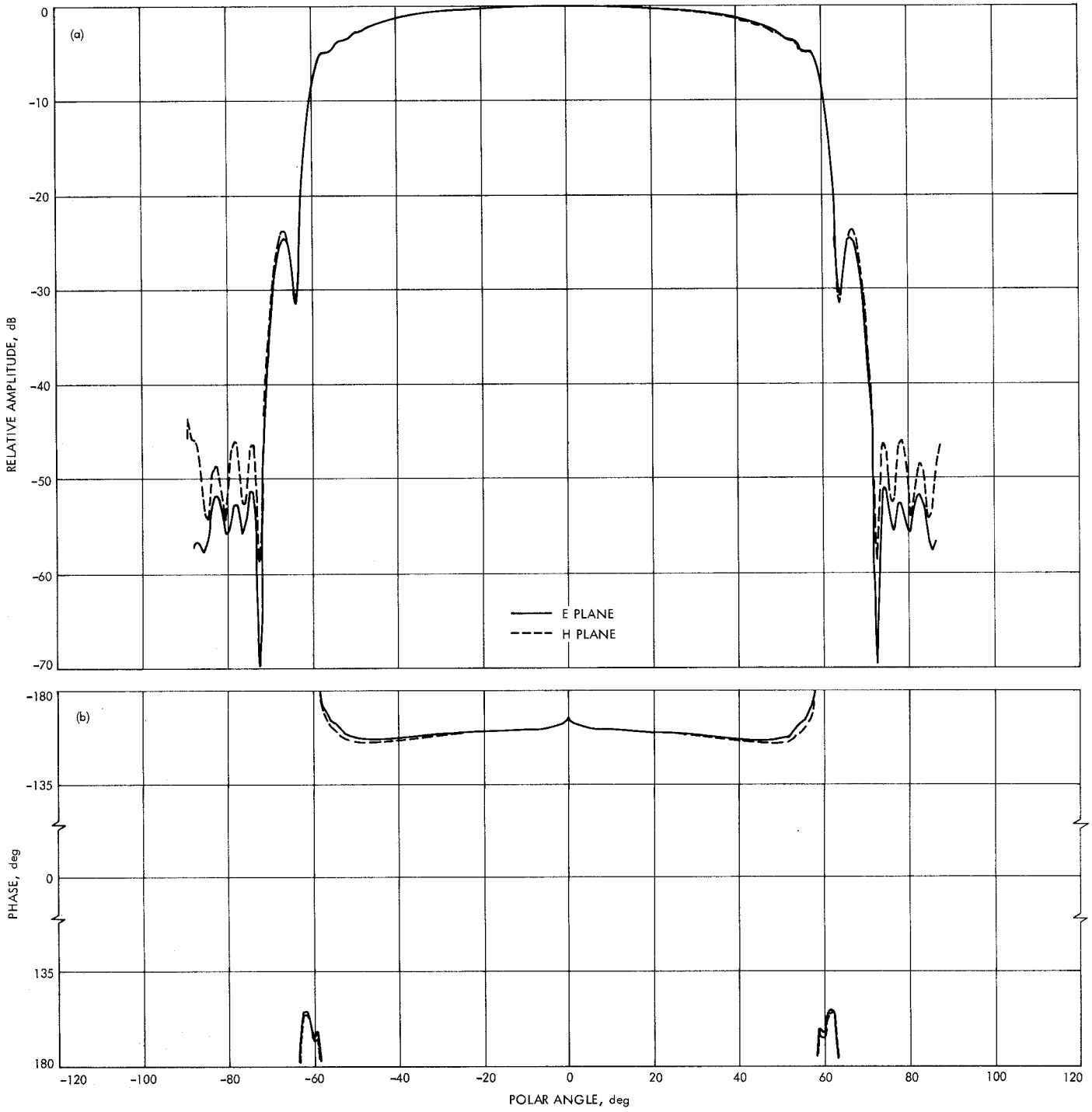

Fig. 12. 2.295-GHz symmetric, shaped system with illuminating aperture scaled by 1.50; (a) amplitude, (b) phase

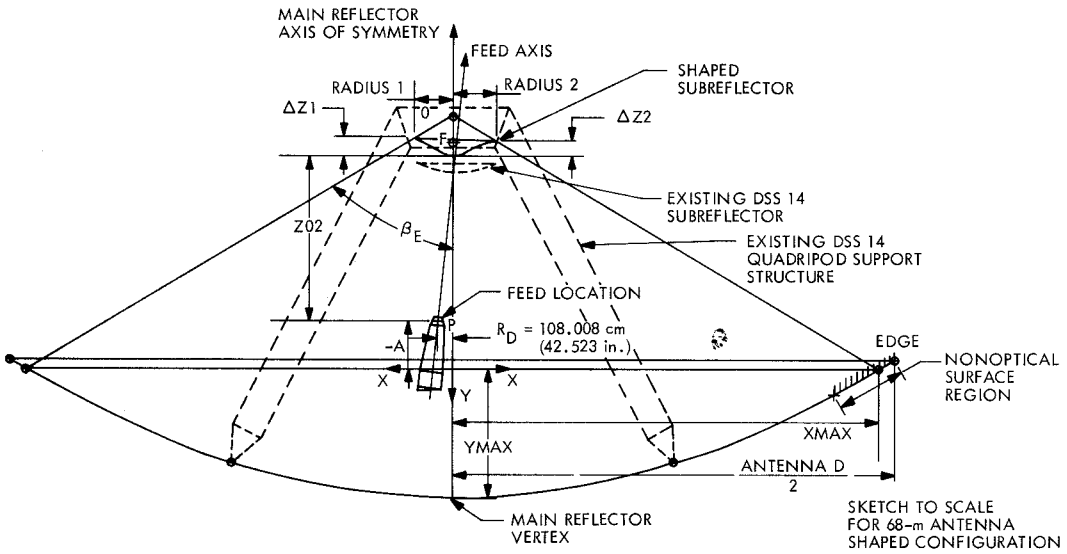

Fig. 13. Shaped antenna mechanical configuration